Supplementary Information

An Organic/inorganic Coating Strategy that Greatly Enhanced Sensing Performances and Reliability of All-fabric Piezoresistive Sensors

Guangliang Tian[a], Kangli Xu[a], Yaoli Huang[a], Xinxin You[a], Wenhua Yu[a], Honggang Liu[b], Juan Li[b], Jiawei Liu[a], Xiangyu Jin[a], Haoxuan Li[c], Qinfei Ke*[a] and Chen Huang*[a,d]*

[a] State Key Laboratory for Modification of Chemical Fibers and Polymer Materials, College of Textiles, Donghua University, Shanghai 201620, China
[b] Tiansheng Nonwoven Technology Co., Ltd., Zhejiang 321035, China
[c] Nonwoven Technology Laboratory, College of Textile Science and Engineering, Jiangnan University, Wuxi, 214122, P. R. China
[d] Henan Key Laboratory of Medical and Protective Products, Henan Yadu Industry Co., Ltd., Xinxiang 453000, China

** Corresponding author.*
E-mail: lihaox@jiangnan.edu.cn
E-mail: kqf@dhu.edu.cn
E-mail: hc@dhu.edu.cn.

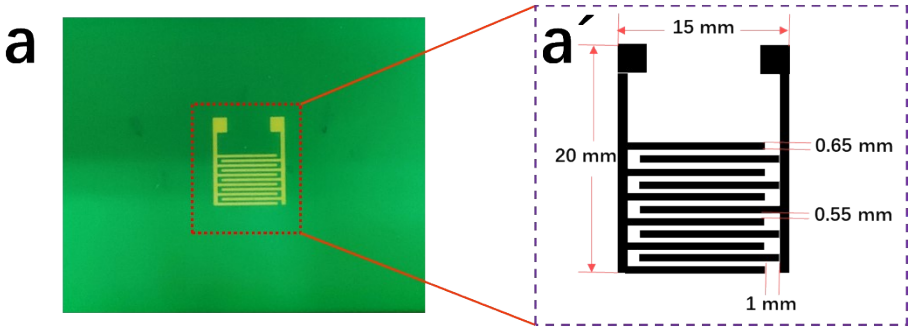

Fig.S1. (a) Photograph of the screen printing plate. (a´) The dimension of the interdigital electrode.

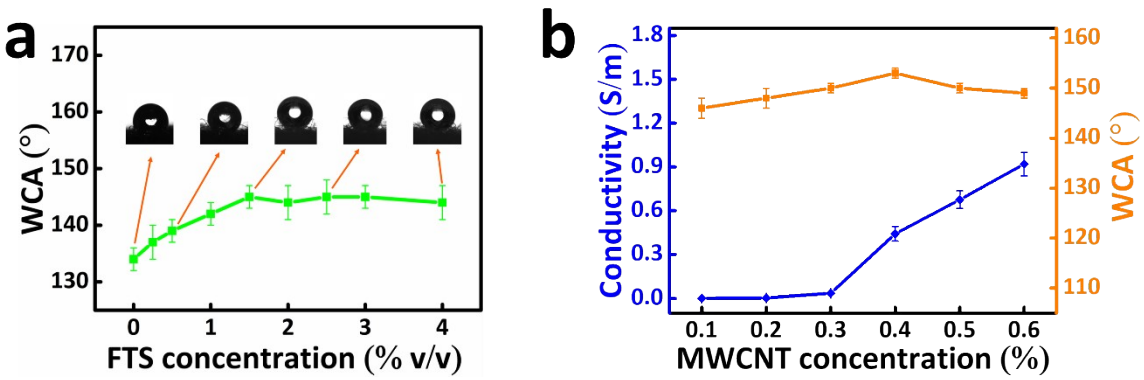

Fig.S2. (a) Influence of FTS concentration on water contact angle (WCA), insets are the digital photographs of WCA. (b) Change of conductivity and WCA with MWCNT concentration.

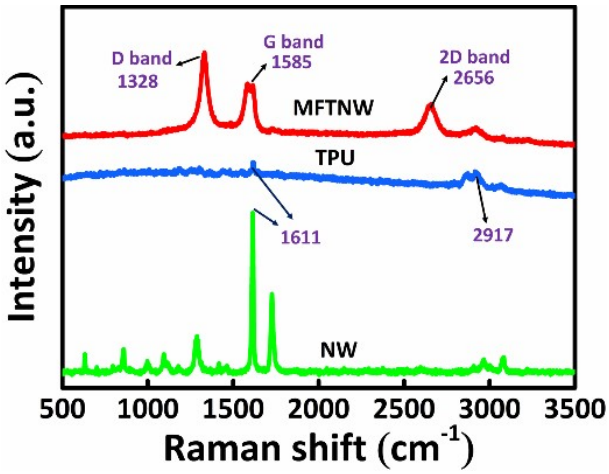

Fig.S3. Raman spectrum of the NW, TPU, and MFTNW.

In the Raman spectrum of MFTNW, the typical characteristic peaks of NW, TPU and MWCNT were obviously identified. The symmetric stretch vibration of C=C (1611 cm^{-1}) and the stretching vibrations of $-CH_2$ (2917 cm^{-1}) of PET and TPU, and the D-band (1328 cm^{-1}), G-band (1585 cm^{-1}) and 2D band (2656 cm^{-1}) of MWCNT were all observed, proving the successful coating of MWCNT and TPU on the NW.

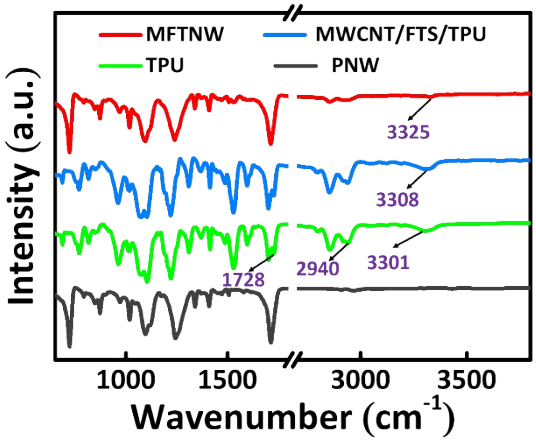

Fig.S4. FT-IR spectra of NW, TPU, MWCNT/FTS/TPU and MFTNW.

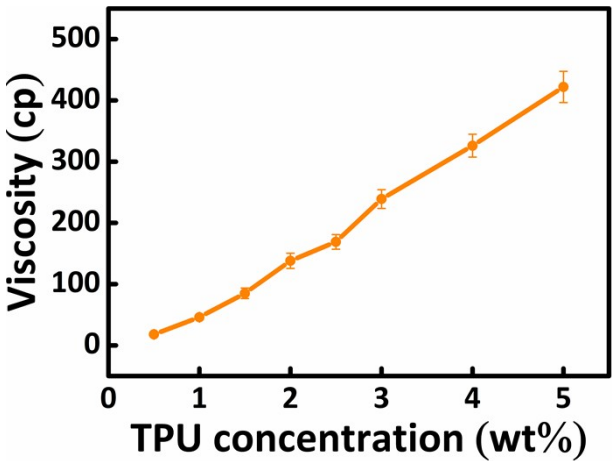

Fig.S5. Influence of TPU concentration on solution viscosity.

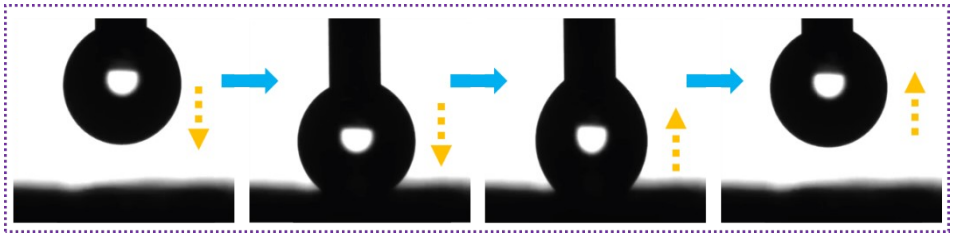

Fig.S6. Digital photograph showing the non-adhesive behavior of MFTNW.

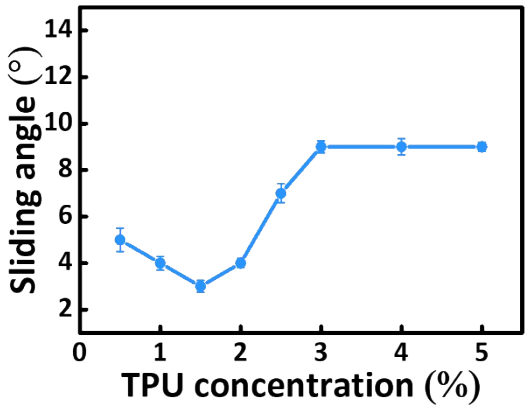

Fig.S7. Sliding angle of the hydrophobic fabric at various concentrations of TPU

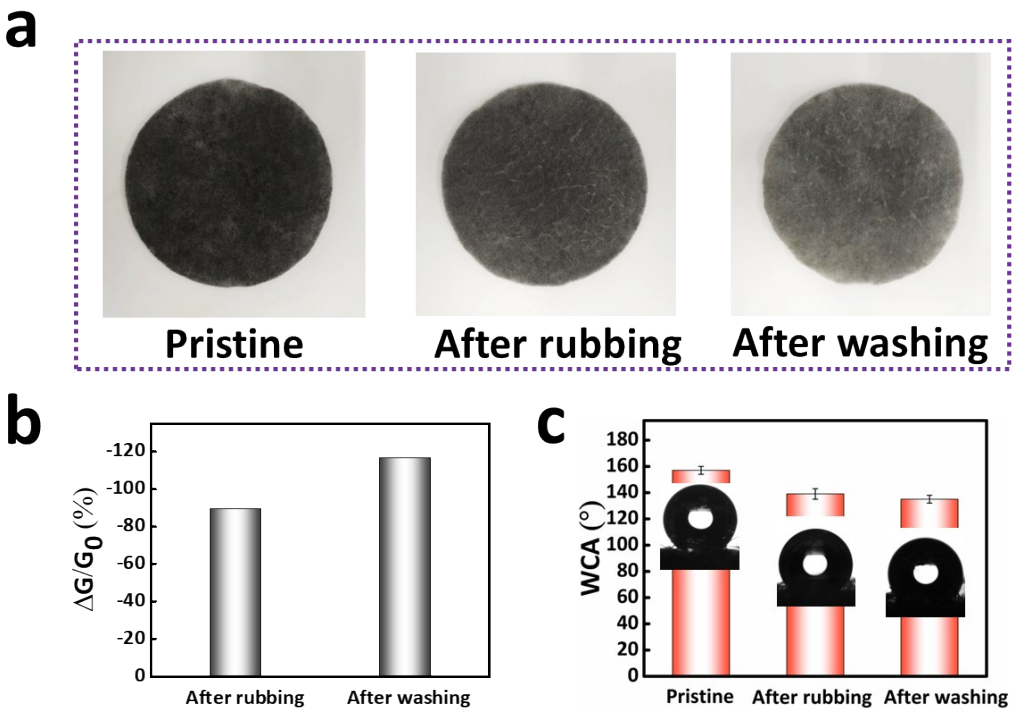

Fig.S8. (a) Photographs of pristine, washed and rubbed NW coated with MWCNT/FTS. (b) Conductivity variation and (c) WCA change of samples after rubbing or washing, respectively.

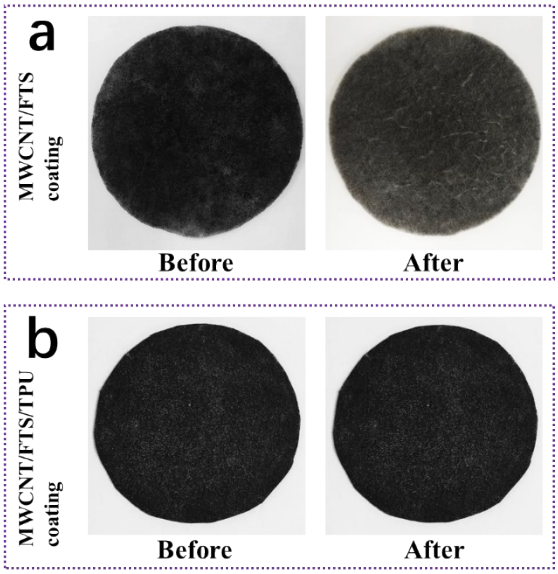

Fig.S9. Photograph of NW coated with (a) MWCNT/FTS and (b) MWCNT/FTS/TPU before and after rubbing.

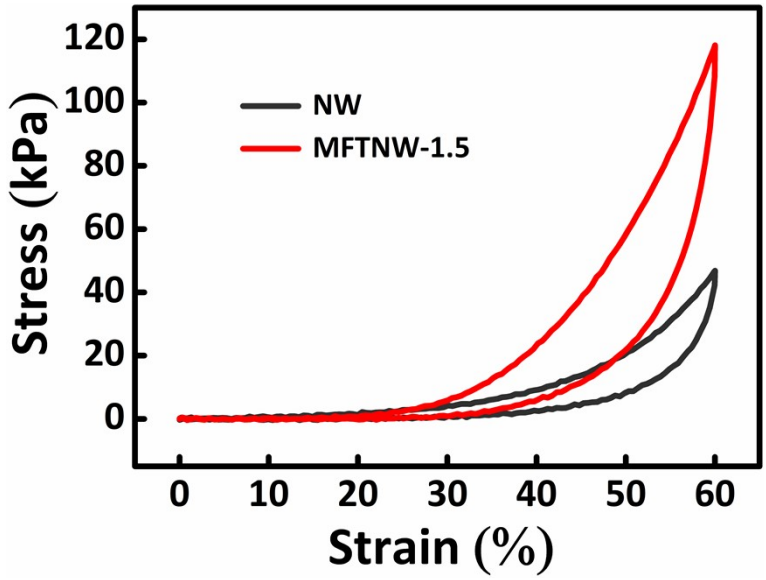

Fig.S10. Stress−strain plots of NW and MFTNW-1.5.

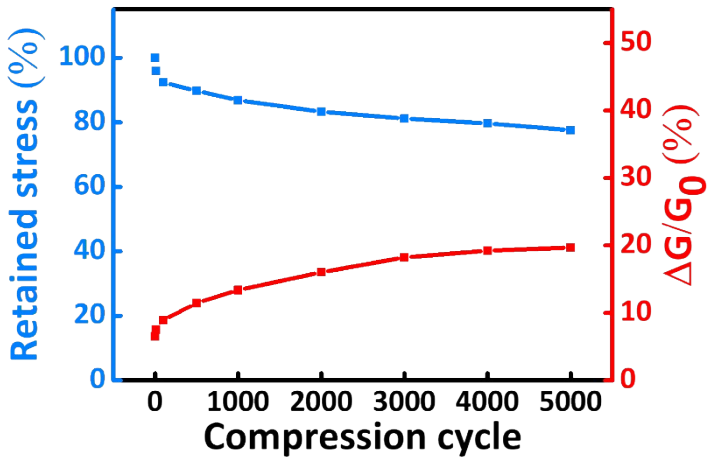

Fig.S11. Retained stress and conductivity of MFTNW after 5000 compression cycles

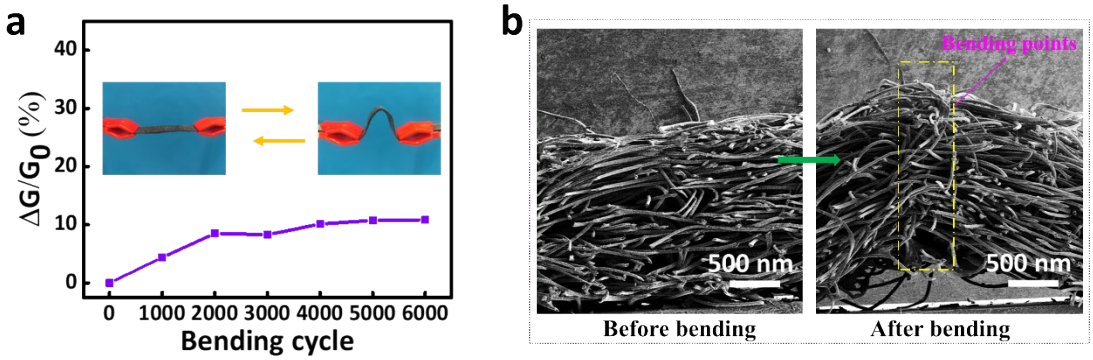

Fig.S12. (a) The relationship between conductivity variation and bending cycles. Insets are photographs showing the bending of MFTNW. (b) SEM images of MFTNW before and after 6000 bending cycles.

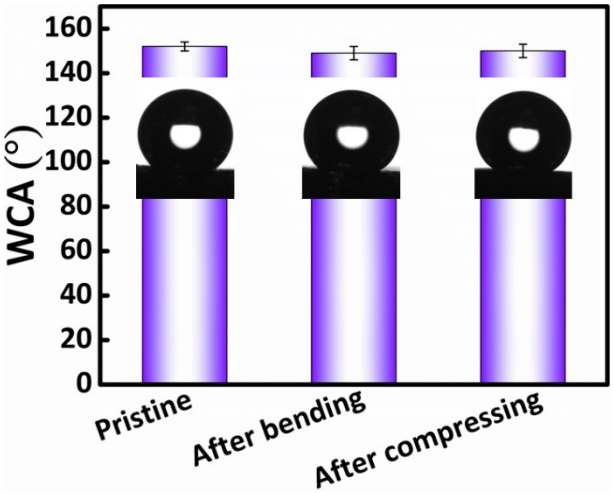

Fig.S13. WCA of MFTNW after bending and compressing.

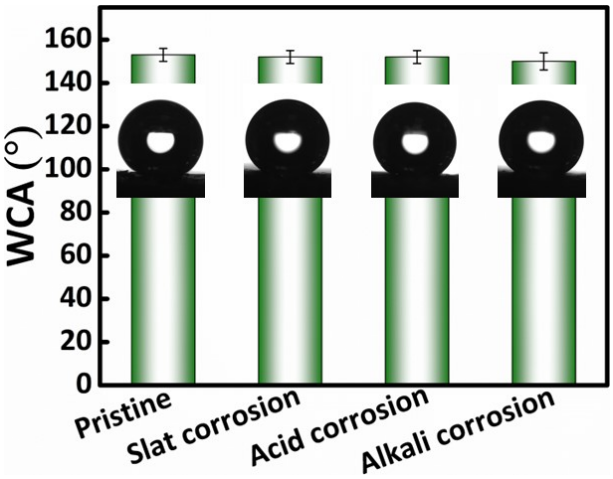

Fig.S14. WCA of MFTNW after slat, acid, and alkali treatment.

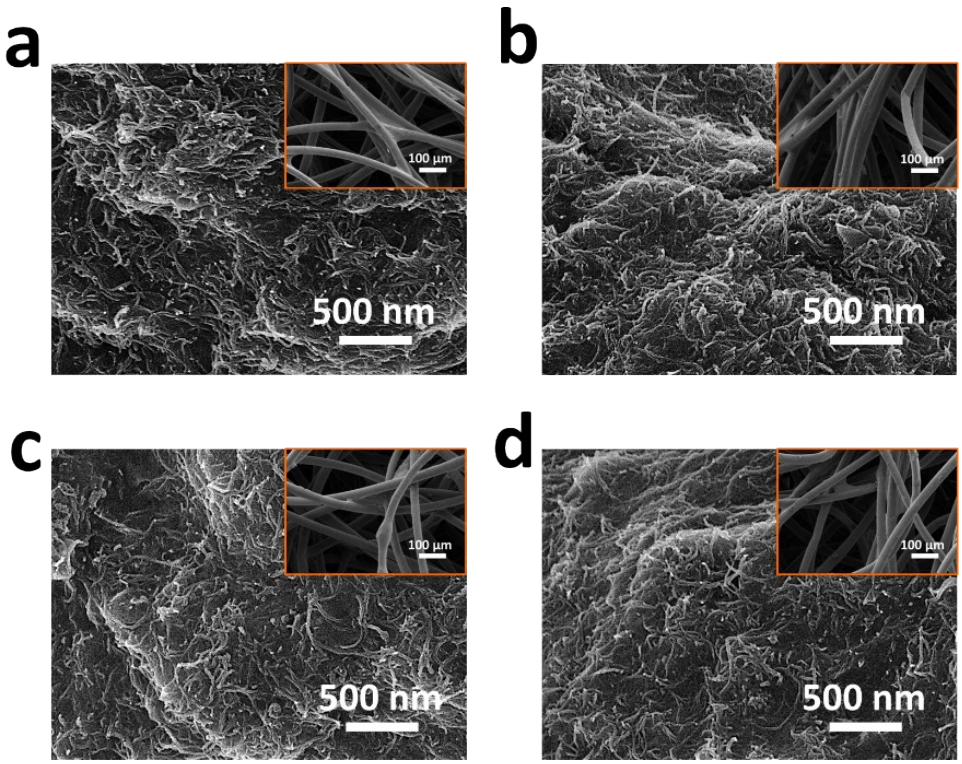

Fig.S15. Surface morphology of (a) pristine MFTNW, MFTNWs after (b) slat, (c) acid and (d) alkali treatment for 28 h.

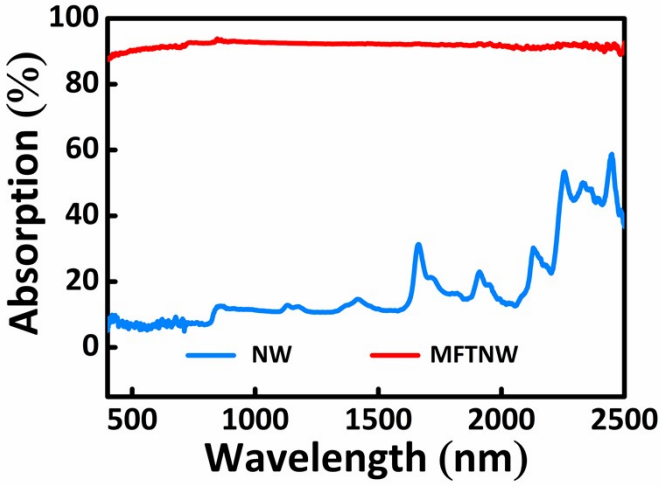

Fig.S16. UV-vis-NIR absorption spectra of NW and MFTNW.

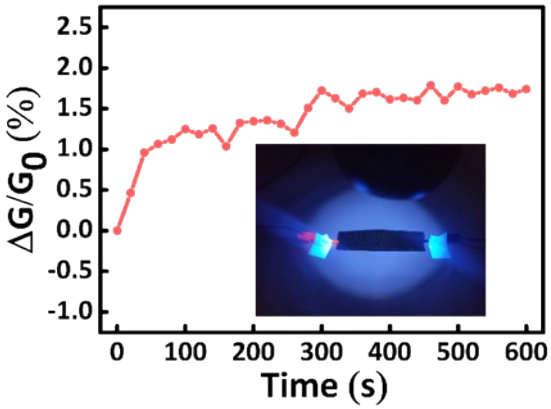

Fig. S17. Change of $\Delta G/G_0$ against irradiating time under ultraviolet light. Inset is a photograph of MFTNW under an ultraviolet lamp.

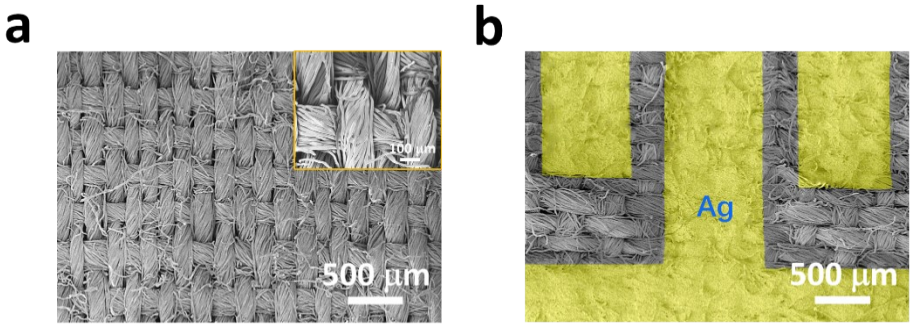

Fig.S18. Surface morphology of (a) cotton fabric and (b) interdigital electrode coated cotton fabric. The interdigital electrode was dyed yellow to intuitively reflect the structure of broken circuit.

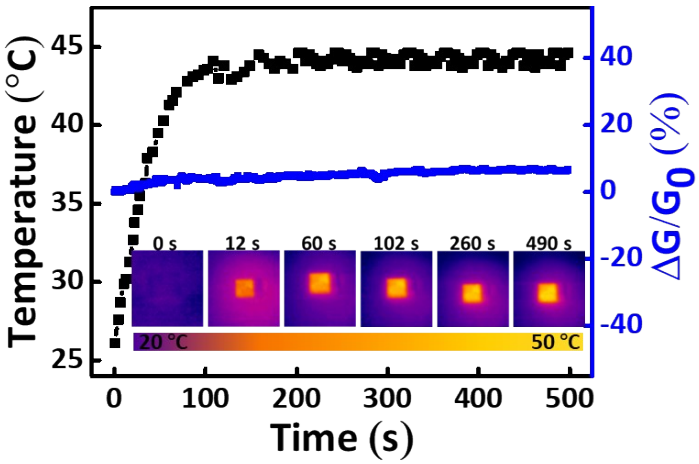

Fig.S19. Change of temperature and $\Delta G/G_0$ against irradiating time under 1 sun. Insets are the typical infrared images of samples at different irradiation periods.

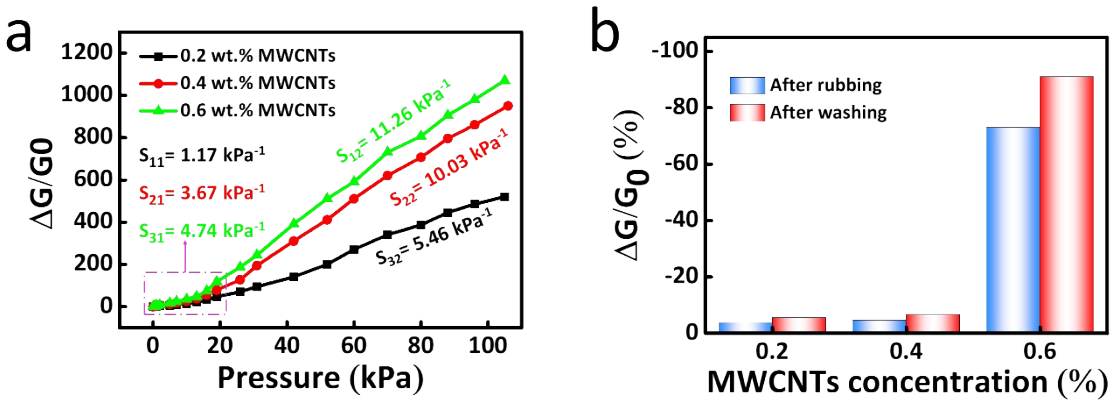

Fig.S20. (a) The relationship between MWCNT concentration and sensitivity of sensors. (b) Conductivity variation of samples after rubbing and washing.

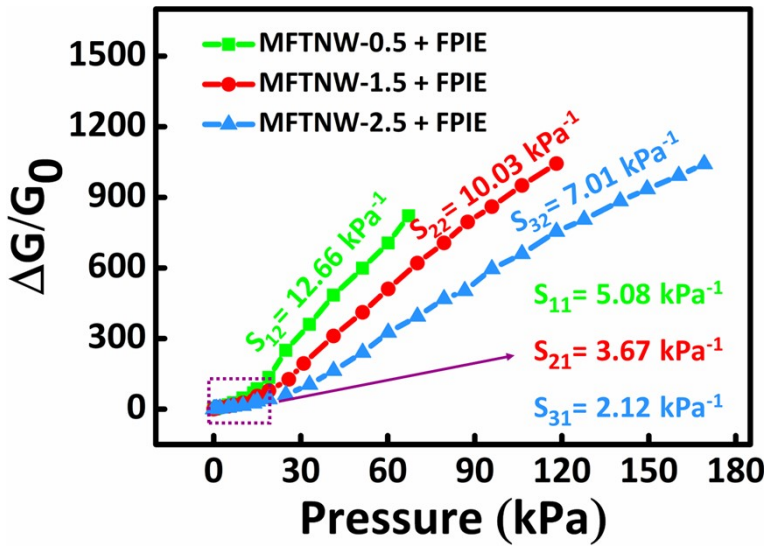

Fig.S21. The relationship between TPU concentration and sensitivity of sensors.

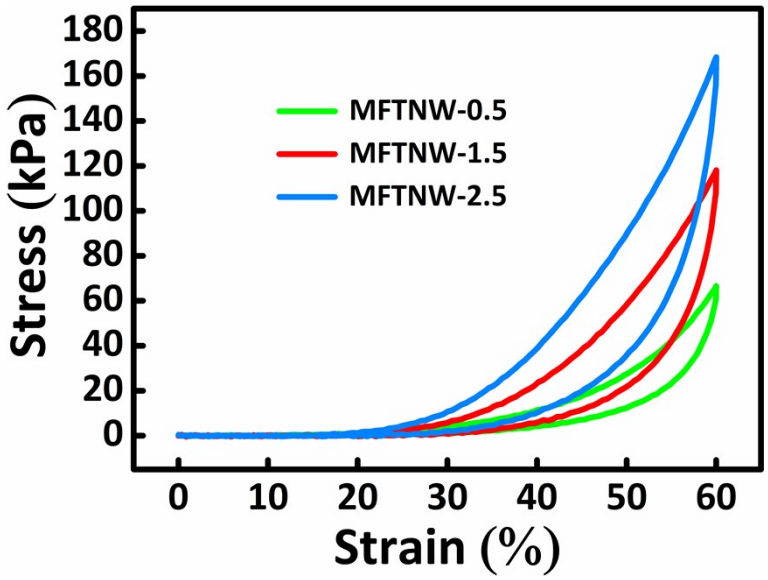

Fig.S22. Stress−strain plots of MFTNW-0.5, MFTNW-1.5, and MFTNW-2.5.

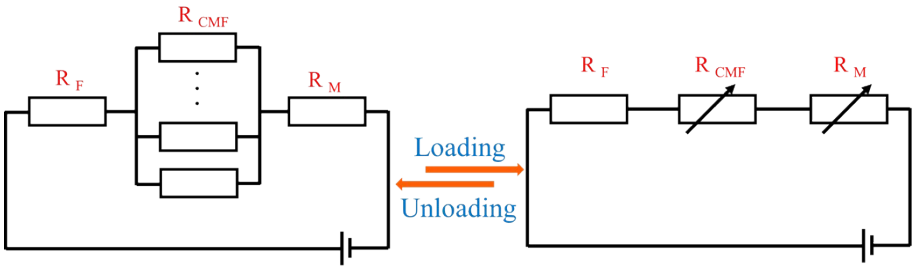

Fig.S23. Schematic diagram of the circuit containing all-fabric piezoresistive sensor (AFPS).

To better understand the working mechanism of our sensor, an equivalent circuit model was established to reveal the resistance variation under pressure. As presented in Fig.S22, total resistance (R_T) of AFPS was composed of three components: the resistance (R_F) of fabric patterned interdigital electrode (FPIE), contact resistance (R_{CMF}) between MFTNW and FPIE, and the resistance (R_M) of MFTNW. As such, R_T of the AFPS was calculated by the following Equation:

$$R_T = R_F + R_{CMF} + R_M \quad (1)$$

As FPIE used in this work was made of highly conductive silver metal, R_F was much smaller than R_{CMF} and R_M. When the pressure was applied, both R_{CMF} and R_M decreased, resulting in a decline in R_T. Thereby, Equation 1 can be simplified as $R_T \approx R_{CMF} + R_M$.

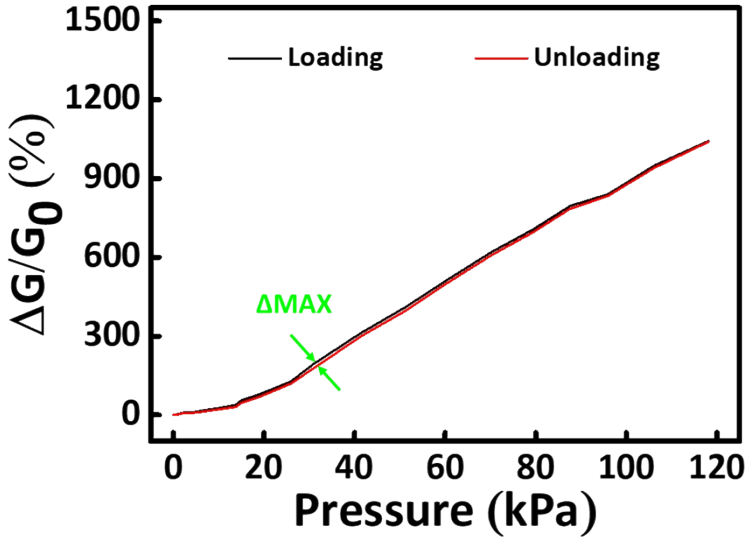

Fig. S24. $\Delta G/G_0$ variation of AFPS during one loading-unloading cycle.

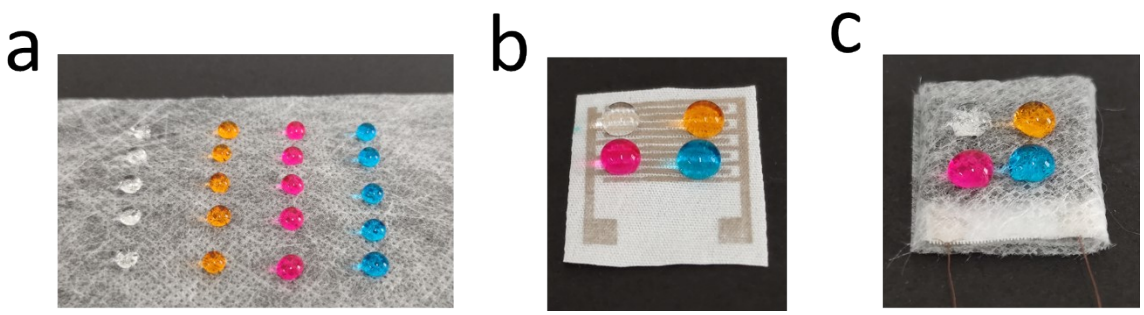

Fig.S25. Hydrophobicity of (a) spunbond NW, (b) FPIE, and (c) sensor.

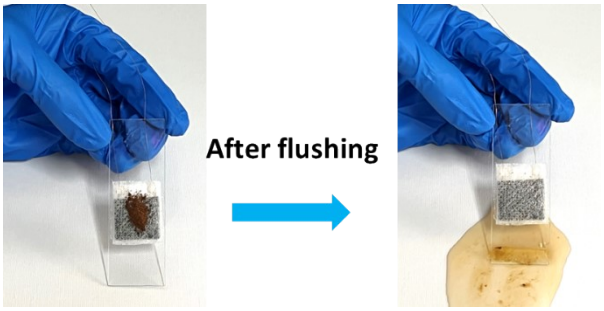

Fig.S26. Photograph demonstrating the easy removal of coffee powders from AFPS.

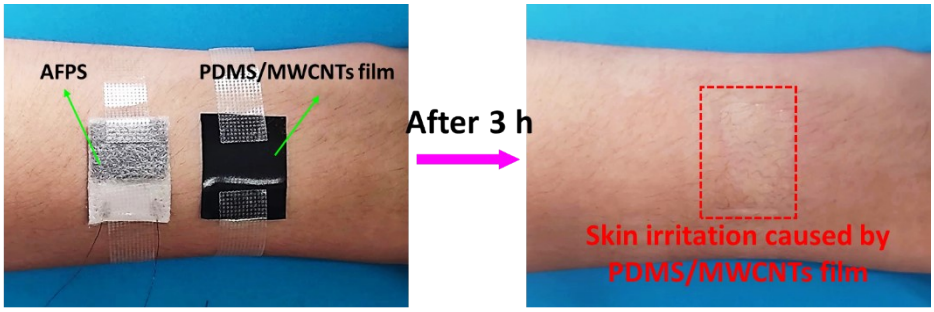

Fig. S27. The images before and after attaching AFPS and PDMS/MWCNTs film on the human skin surface for 3 h.

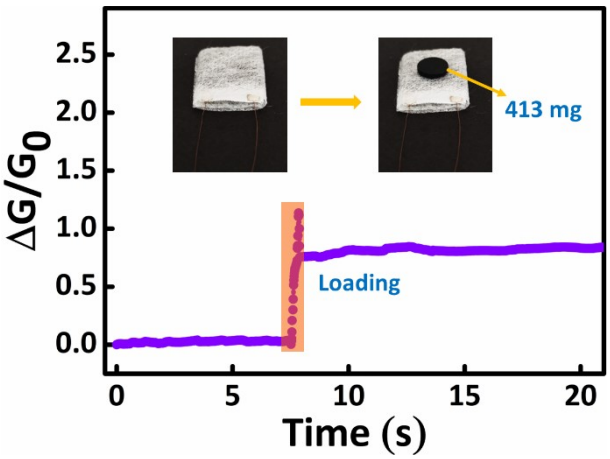

Fig.S28. $\Delta G/G_0$ signals resulted from the weight of 413 mg.

When an object weighing 413 mg (~210 Pa) was placed on the sensor, an increased $\Delta G/G_0$ value could be observed. This proved that AFPS was capable of detecting small pressure (<0.5 kPa).

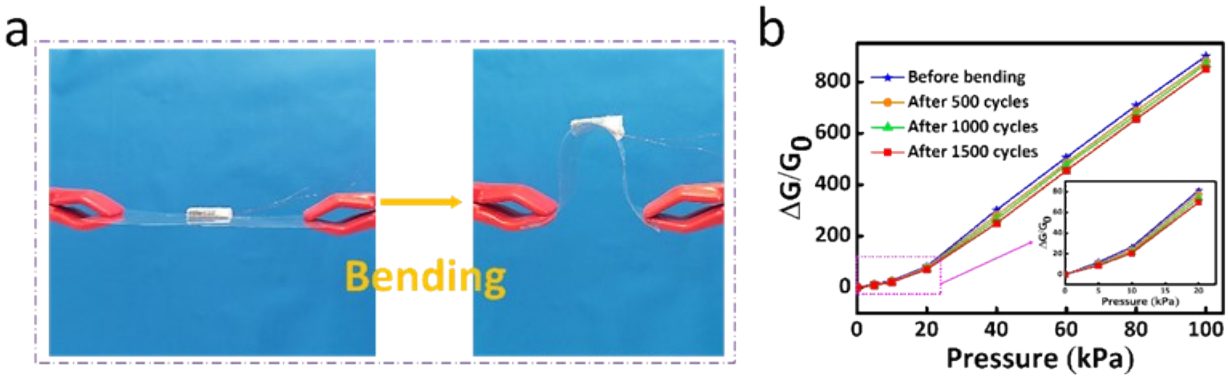

Fig.S29. (a) photographs showing the bending of sensor. (b) Pressure-response performance of sensor before and after 1500 bending-releasing cycles.

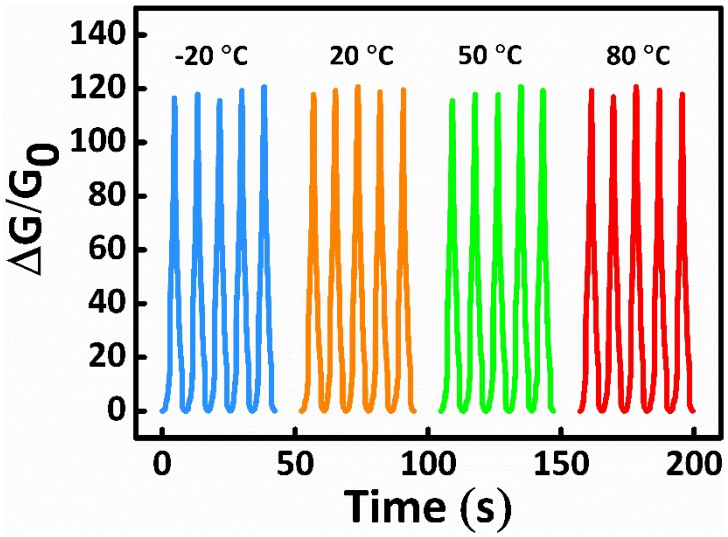

Fig. S30. $\Delta G/G_0$ variations of AFPS during cyclic compression under different temperature.

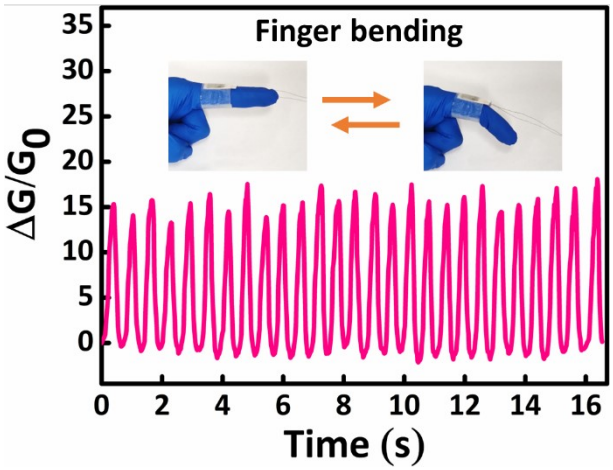

Fig.S31. $\Delta G/G_0$ signals induced by forefinger bending. Insets are photographs showing a sensor-loaded glove for detecting forefinger bending signals.

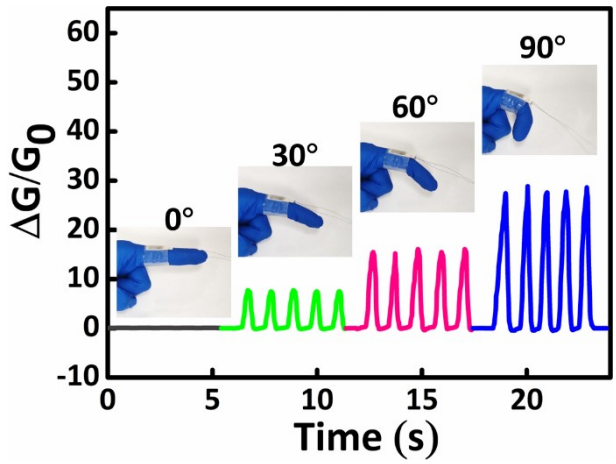

Fig.S32. $\Delta G/G_0$ signals caused by different bending angles of forefinger.

Movie S1. Video presenting low adhesion of MFTNW to water.

Movie S2. Video showing wireless transmission of sensor output signal.